Karki, Sabin Kumar; Ala-Laurinaho, Juha; Viikari, Ville

Low-Profile Scanloss-Reduced Integrated Metal-Lens Antenna

Published in:
IEEE Transactions on Antennas and Propagation

DOI:
10.1109/TAP.2021.3111192

Published: 01/02/2022

Document Version
Publisher's PDF, also known as Version of record

Low-Profile Scanloss-Reduced Integrated Metal-Lens Antenna

Sabin Kumar Karki, *Student Member, IEEE*, Juha Ala-Laurinaho, and Ville Viikari, *Senior Member, IEEE*

***Abstract*— Integrated lens antennas are widely used in high gain and beam steering applications at millimeter-wave frequencies. The ILA has often large height and suffers from significant scan loss. In this article, we demonstrate a low-profile, efficient, and scanloss-reduced integrated metal-lens antenna (IMLA). An IMLA is a combination of a dielectric lens and metal–plate lens. A 16-λ_0 diameter IMLA is designed using the HDPE and 58 stainless steel plates to achieve the f/d of 0.69. The simulated aperture and radiation efficiency of the IMLA are 73% and 92%, respectively. At 76 GHz, the simulated and measured realized gains of the fabricated IMLA are 31.24 and 31 dBi, respectively. The IMLA is designed to steer the main beam to ±30°. The scan loss is reduced by tilting the radiation pattern of the feeds at offset positions along the focal plane. The radiation pattern of the square waveguide feed is tilted using asymmetrical dielectric pins. The asymmetrical dielectric pins reduce the simulated gain scan loss of the IMLA by more than 1.5 dB at 30° steering angle. The simulation results show that the inclination of the feed radiation pattern helps limit the scan loss of the IMLA to 4.1 and 4.3 dB in the H- and E-planes for 30° steering angle, respectively. The measured scan loss of the manufactured IMLA is 3.8 and 6.2 dB in the H- and E-plane, respectively.**

***Index Terms*— Antenna, beam switching, beam tilt, dielectric lens antenna, high gain antenna, low-profile lens, matching layers, metal–plate lens, millimeter-wave frequencies, scan loss reduction.**

I. Introduction

AN INTEGRATED lens antenna (ILA) is a shaped dielectric material combined with the radiating elements. The operation and design principles of a homogenous ILA have been thoroughly investigated, for example, in [1] and [2]. An ILA is a popular choice for the high gain and beam steering applications [3]. The renewed interest on ILA can be associated with the utilization of the high frequencies for communication system, imaging, and radar applications [4], [5]. An ILA with beam-switching feeds along the focal plane has been widely studied for a point-to-point radio link of the communication system [6]–[8]. The major drawbacks of an ILA are gain reduction with increasing steering angle, bulky dimensions, and dielectric and spillover losses. The drawbacks of an ILA can mostly be associated with a single parameter, the focal length. When the focal length/height of an ILA decreases, the extension section also decreases which leads to lower spillover loss [9]. The dielectric loss depends on the dimensions and loss tangent of the dielectric material. The smaller focal length results in lower dielectric loss. Thus, the shorter focal length improves the efficiency of an ILA. Furthermore, the shorter the focal length, the more appealing is the appearance for the practical applications.

Numerous research activities have been conducted to minimize the height of an ILA. The focal length to diameter ratio, f/d, of an ILA is inversely proportional to the relative permittivity of the material. High relative permittivity materials like PREPERM L450 ($\epsilon_r = 5.01$), alumina ($\epsilon_r = 9$), and silicon ($\epsilon_r = 12$) are used to shorten the focal length [1], [10], [11]. However, the high-permittivity materials are typically expensive and lossy, have high density, and are difficult to tool. The gradient index (GRIN) lens or multimaterial are used to design low-profile lenses [12]–[14]. It is difficult to find the combination of low loss materials with desired relative permittivities [13]. The fabrication of a GRIN lens using the single material is challenging at higher frequencies [12]. A complex 3D collimating shape of the lens can reduce the focal distance [15]. An air cavity is introduced at the feed plane of an ILA and it helped to reduce focal length by 13% [16]. The design reduces the efficiency of the ILA due to multiple reflections caused by the cavity. A folded Fresnel zone plate lens is designed with 0.225 f/d [17]. The design supports single polarization and beam steering is not possible. A 2 × 2 elliptical ILA array is designed in [18] to half the focal length when compared to a traditional ILA. In most of the low-profile ILA solutions, the beam steering characteristics and scan loss have not been discussed [15]–[18].

The idea of a low-profile lens based on the combination of a dielectric and a metal–plate lens, that is, the integrated metal-lens antenna (IMLA), is presented in [19]. With this approach, the focal length of the low relative permittivity materials, like Teflon, can be minimized by approx. 35% when compared to a traditional elliptical ILA.

The steering angle of an ILA is determined by the offset position of the feed from the focal point [2]. The scan loss of an ILA is mainly contributed by the reduction of the effective radiating aperture with increasing steering angle, the increase in internal reflections at the dielectric–air interface with larger offset position, the offset between the planar feed plane and ideal focal arc, and unequal amplitude distribution along the radiating aperture with increasing offset position.

Manuscript received September 21, 2020; revised August 2, 2021; accepted August 5, 2021. Date of publication September 15, 2021; date of current version February 3, 2022. This work was supported in part by the Business Finland through the 5WAVE Project and in part by the Academy of Finland through the ADENN Project. The work of Sabin Kumar Karki was supported in part by the Nokia Foundation and in part by the Walter Ahlström Foundation. *(Corresponding author: Sabin Kumar Karki.)*

The authors are with the Department of Electronics and Nanoengineering, School of Electrical Engineering, Aalto University, 00076 Espoo, Finland (e-mail: sabin.karki@aalto.fi).

Color versions of one or more figures in this article are available at https://doi.org/10.1109/TAP.2021.3111192.

Digital Object Identifier 10.1109/TAP.2021.3111192

In [20], at higher steering angles, the decrease in effective radiating aperture of an ILA was compensated by increasing the physical aperture. The internal reflections at dielectric–air interface is lowered in [21] by shortening the length of the extension section, thereby decreasing the scan loss. In [13], a 0.785 f/d double-shell ILA is designed with MACOR, $\epsilon_r = 5.5$, and acrylic, $\epsilon_r = 2.53$, materials to steer the main beam to $\pm 20^\circ$ with 0.4-dB scan loss. The high dissipation losses of the materials degrade the radiation efficiency by approx. -6.2 dB. A double lens focusing system is proposed in [22], which reduces the aberration of a hemispherical ILA and limits the scan loss below 1.2 dB for a $\pm 30^\circ$ steering angle.

The feed elements can be placed along the focal arc rather than focal plane to reduce the aberration and improve the feed orientation [23], [24]. A dual-spherical ILA with 1×16 beam-switching array was proposed in [25]. The dual-spherical ILA limits the scan loss to 1.2 dB within $\pm 40^\circ$ scanning range. Positioning of feed along the arc for 2-D beam-steering application is challenging. The off-axis performance of an ILA can be improved by tilting the radiation pattern of the feed at offset positions [26]. With the approach, all feed antennas along the focal plane must be unique based on its location from the focal point. The tilting of the radiation pattern depends on the antenna performance and it is likely to be narrow band. Recently, the tilting of the feed radiation pattern is implemented using the dielectric grating with modulated height in the extension section of an elliptical ILA [27]. The design improved the scan loss by 4 dB for 25° steering angle along the H-plane. In this work, we propose to tilt the feed radiation pattern using a common feed antenna along the focal plane in both the E- and H-planes. The beam tilting can achieved by introducing the asymmetric dielectric pin corrugated along the focal plane of the dielectric lens and the radiation pattern tilting is achieved in a full WR-12 band, 60–90 GHz.

The objective of the article is to design an efficient low-profile integrated metal-lens antenna (IMLA) with reduced scan loss. The novelty of the work relies on the design, fabrication, and characterization of the IMLA of 16-λ_0 diameter at lower E-band, that is, 71–76 GHz. The design method of the IMLA and its matching layers are illustrated in detail. The IMLA is designed to steer the main beam until $\pm 30^\circ$. A unique wideband beam tilting technique of a square waveguide feed in both the E- and H-planes are demonstrated. In addition, the scan loss reduction based on feed radiation pattern tilting is demonstrated in this article. The fabrication challenge and their effects on the IMLA performance are also analyzed.

The article is organized as follows. In Section II, the IMLA and its operation are described. The same section also illustrates different matching layers and their design methods. The beam tilting method of the square waveguide feed and improvement in the IMLA performance is demonstrated in Section III. Section IV presents the comparison of the IMLA performance with the state of art. The fabrication, characterization, and result analysis of the IMLA can be found in Section V. Finally, the conclusions are presented in Section VI.

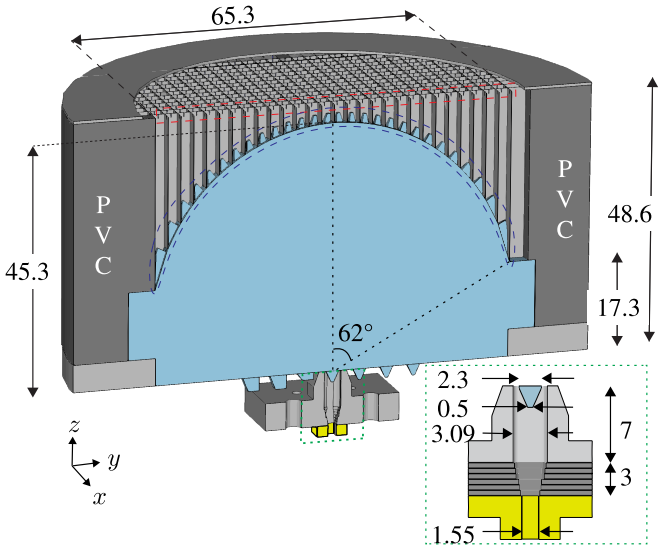

Fig. 1. Orthographic view with the E-plane cut of the IMLA showing the dielectric–metal (blue dashed line) and waveguide–air (red dashed line) matching layers. The inset shows the yz cross-section view of the square waveguide (light grey), waveguide–lens dielectric pin (blue), the transition plates (dark grey), and WR-12 waveguide (yellow). Dimensions are in mm.

II. Integrated Metal-Lens Antenna Design

The operation principle and design method of an IMLA are introduced in [19]. The integrated metal-lens antenna (IMLA) is a combination of the dielectric lens and metal–plate lens [28], as shown in Fig. 1. Based on the principle of path length equality, the dielectric–metal interface can be designed using the equation

$$(\epsilon_r - \epsilon_m)y^2 + 2\sqrt{\epsilon_r} f(\sqrt{\epsilon_r} - \sqrt{\epsilon_m})y + \epsilon_r z^2 = 0 \qquad (1)$$

where f is the focal length, ϵ_r is the relative permittivity of the dielectric material, and ϵ_m is the effective permittivity of the metal–plate region. The effective permittivity of the metal–plate lens is given by the equation $\epsilon_m = 1-(\lambda_0/(2a))^2$, where a is the separation distance between the parallel plates and λ_0 is free space wavelength. Since the ϵ_m is a function of frequency, the operation bandwidth of the IMLA is limited [28].

The aim of this work is to design a low-profile IMLA. As explained in [19], the focal length of an IMLA can be reduced by using large gradient of relative permittivity between the dielectric and metal–plate lens region. The dielectric lens is designed using high-density polyethylene (HDPE) ($\epsilon_r = 2.31$ and $\tan\delta = 0.0002$ at 73 GHz) material. The HDPE is chosen because the height reduction of an IMLA is more effective with low relative permittivity materials, that is, $2 < \epsilon_r < 5$ [19]. The low loss tangent of HDPE at higher frequencies is another reason for the selection.

The metal–plate lens with smaller effective ϵ_m decreases the IMLA's focal length. The smaller effective ϵ_m is achieved by reducing the separation between the metal plates. Ideally, the parallel plates operate when the separation a between them is greater than $0.5\lambda_0$. However, when $a < 0.55\lambda_0$, the wave impedance is large and the reflections in the dielectric to

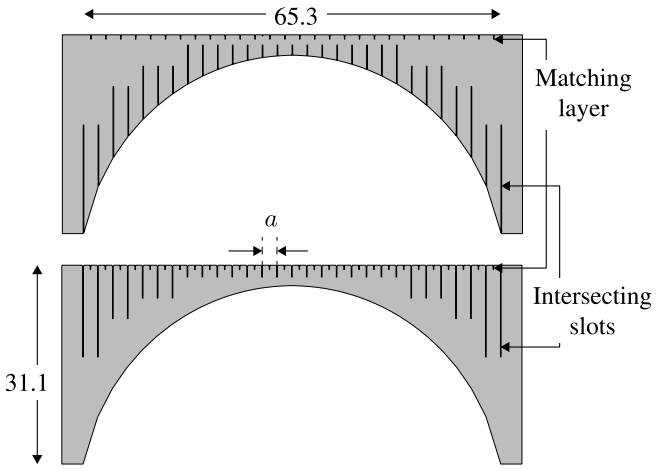

Fig. 2. 2D CAD drawing of the center plates placed along the orthogonal direction/planes of the metal–plate lens. Dimensions are in mm.

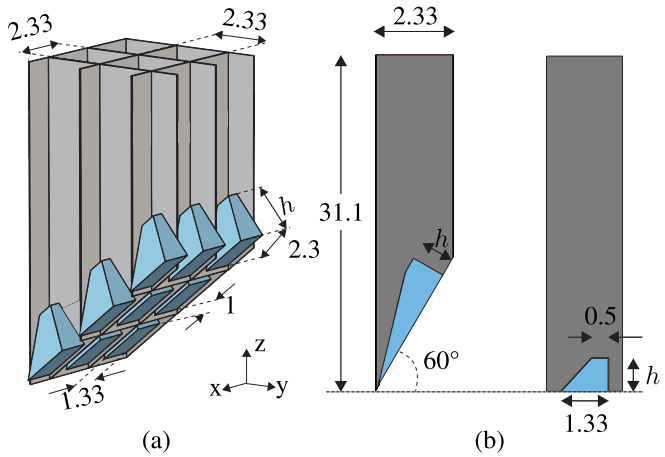

Fig. 3. (a) Orthographic view of the simulation model of a waveguide array, $\theta_o = 45°$, to design the dielectric pin for the matching layer in the interface between dielectric and metal–plate lens and (b) cross-section (yz-cut) view of the center waveguide with $\theta_o = 60°$ and 0°. Dimensions are in mm.

metal–plate lens and metal–plate lens to air interfaces become significant. Therefore, the metal–plate separation of $0.56\lambda_0$ at 73.5 GHz is used in the design. The effective permittivity of the metal–plate lens region is 0.2.

The metal–plate lens is designed by intersecting the 50-μm-thick stainless steel ($\sigma = 7.7 \times 10^6$ S/m) plates in orthogonal directions. A total of 58 stainless plates, 29 along the YZ-plane and 29 along the XZ-plane, are interleaved in orthogonal direction to form the metal–plate lens. The primary purpose of positioning the plates in orthogonal directions is to enable dual-polarized operation. An added benefit of having plates in orthogonal direction is to correctly position the plates and improve the sturdiness of the metal–plate lens. Ideally, the plates along one direction can enable single polarization, however the plate thickness of 50 μm is not rigid enough to maintain the uniform plate separation distance. In order to facilitate the interleaving, the intersecting slots are laser cut in each plate. The slots of plates in the XZ-plane are at the dielectric lens end, whereas those on the YZ-plane are at the air interface end (see Fig. 2). The width of the slots is equal to the thickness of the stainless steel, that is, 50 μm. The length of the slots is increased based on its position from the axis.

An IMLA of 16-λ_0 diameter is designed in this work to operate in the lower E-band, that is, 71–76 GHz. The focal length f of the designed lens is $11.1\lambda_0$. The f/d ratio of the IMLA with and without the matching layers are 0.74 and 0.69, respectively. The length of the extension section is 17.3 mm. The angle between the focal axis and the line from the focal point to the edge of the metal–plate lens is 62° (see Fig. 1).

The large contrast of the relative permittivity between dielectric and metal–plate lens region and, further, between the metal–plate lens and air leads to significant reflections in the corresponding interfaces. Therefore, appropriate matching layers are required to improve the IMLA performance.

A. Dielectric–Metal Matching Layer

The difference in relative permittivity of the dielectric lens ($\epsilon_r = 2.31$) and metal–plate lens ($\epsilon_m = 0.2$) causes the impedance mismatch which leads to reflection. The intersecting plates of the metal–plate lens form array of waveguide like structures with wall-to-wall width a of 2.28 mm. A dielectric pin-based matching layer is designed for a waveguide to minimize the reflections. The right trapezoidal-shaped dielectric pins are corrugated on the surface of the dielectric lens as shown in Fig. 1. The dielectric pins are designed to inset inside the waveguides. At the dielectric and metal–plate interface of the designed IMLA, the opening angle of a waveguide θ_0 varies from 0° to 70° based on the lateral distance from the axis. The right trapezoid shape of the dielectric pin is maintained for all opening angles θ_0 to ease the machining process.

The matching layer is designed by minimizing the active reflection coefficient $|S_{11}|$ of the square waveguide radiating into the HDPE background. The waveguide is simulated in 3×3 waveguide array configuration where all elements have the same θ_0 as shown in Fig. 3(a). All the waveguides are simultaneously excited using waveguide ports. $|S_{11}|$ is minimized for the waveguide θ_0 from 0° to 70°. The array is simulated using the full-wave simulation in CST Microwave Studio.

The simulation results indicated that the low $|S_{11}|$ can be achieved with smaller top width and wider bottom width of the right trapezoid dielectric pin. The top width of the dielectric pin is selected to be 0.5 mm considering the manufacturing feasibility. The machining process requires a minimum separation of 1 mm between the adjacent dielectric pins at the base. With increasing θ_0, the width of the base changes as $a/cos(\theta_0) - 1$, whereas the top width remains the same, 0.5 mm. The $|S_{11}|$ of the center square waveguide of the 3×3 array is minimized by varying the height h of the dielectric pin. Based on the parametric sweep, the height of 1.8 mm of the dielectric pin gives the optimal $|S_{11}|$ for all θ_0 of the waveguide (see Fig. 4 for optimal case performance). $|S_{11}|$ is also monitored for the various steering angles along the direction of waveguide opening, that is, the yz-plane, by changing the excitation phase of neighboring waveguides. Fig. 4 also shows that $|S_{11}|$ does not degrade when the

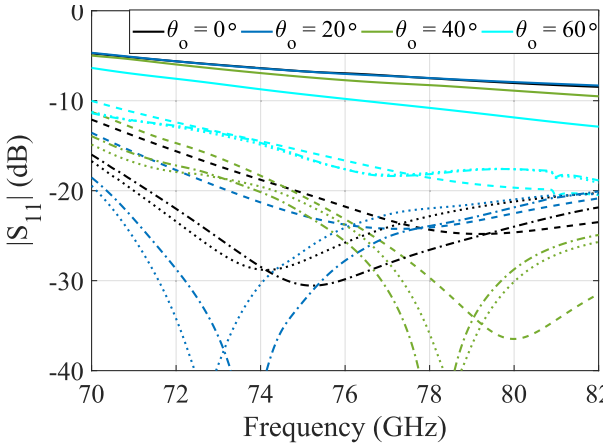

Fig. 4. $|S_{11}|$ of the center waveguide without dielectric pin (—), with dielectric pin, and 0°(- -), 40°(· · ·), and 80°(-.-) phase difference between the neighboring elements for various θ_0 of the waveguide.

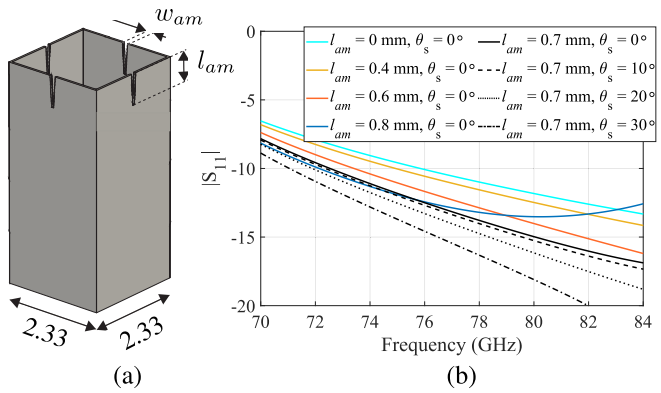

Fig. 5. (a) Unit-cell simulation model of the waveguide and (b) active reflection coefficient of the waveguide w.r.t. matching slot length, l_{am}, and steering angle, θ_s, when the slot width $w_{am} = 0.135$ mm. Dimensions are in mm.

neighboring waveguides have different excitation phase. For both the positive and negative steering angles along the yz-plane, the effect on $|S_{11}|$ is similar.

B. Metal–Plate Lens to Air Matching Layer

At the interface between the metal–plate lens and air, the metal–plate lens can be considered as 2D array of square waveguides. Hence, a square waveguide of 2.28 mm inner width is simulated in a unit cell with periodic boundary conditions. The IMLA is designed to steer the beam to ±30°, and therefore the active reflection coefficient, $|S_{11}|$, of the square waveguide up to the desired steering angle is simulated and minimized.

The unit-cell model of the waveguide with the proposed matching layer is shown in Fig. 5(a). $|S_{11}|$ of the open-ended square waveguide radiating toward free space is minimized by placing the inverted pyramidal slots in the waveguide walls at the radiating aperture of the waveguide. The slots are placed at the center of the waveguide wall. The opening width w_{am} and the length l_{am} of the slot are varied to minimize the reflection. The waveguide is close to cut-off frequency, and therefore $|S_{11}|$ is high at lower frequency. According to simulation results, the bottom width of the slot is desired

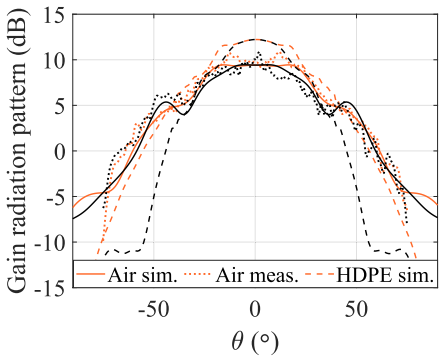

Fig. 6. H-plane (orange) and E-plane (black) radiation pattern comparison of the square waveguide radiating into free space and HDPE at 74 GHz.

to be as small as possible. The bottom width of 50 μm is selected based on the minimum cutting gap of the laser-cutting facility. In Fig. 5(b), $|S_{11}|$ of the unit-cell model is presented for various length of the slot. When the l_{am} and w_{am} are 0.7 and 0.135 mm, respectively, the $|S_{11}|$ decreases more than 3 dB when compared to a waveguide without matching, that is, when $l_{am} = 0$. When the beam is steered, $0° < \theta_s < 30°$, the $|S_{11}|$ of the waveguide further improves.

C. Square Waveguide Feed

A square waveguide of 3.09 mm aperture length corresponding to the standard WR-12 waveguide width is used as a feed antenna. A square waveguide is chosen to fit the dielectric pins, which will be explained in the later section. The square waveguide is manufactured of aluminum ($\sigma = 3.8 \times 10^7$ S/m). The corners of the waveguide are blended with the radius of 1 mm. The simulated and measured radiation patterns of the square waveguide radiating into free space shows close agreement (see Fig. 6).

1) WR-12 Rectangular-Square Transition: During measurements, the square waveguide is connected to a PNA through E-band extension which has a rectangular WR-12 waveguide output. The cross-section width and height of the rectangular WR-12 waveguide are 3.09 and 1.545 mm, respectively. In order to minimize the reflection between the rectangular and square waveguides, a transition is required. The transition is designed by gradually increasing the cross-section height of the rectangular waveguide as shown in Fig. 1. The transition is implemented by adding six laser-cut stainless steel plates between the rectangular and square waveguides. The thickness of each metal plate is 0.5 mm. The rectangular holes with the constant width, that is, 3.09 mm, and increasing height h_t are laser cut in the plates. The height of the rectangular holes in the transition plates starting with the one close to the WR-12 rectangular waveguide are 1.7, 1.87, 2.03, 2.52, 2.63, and 2.85 mm, respectively. The simulated and measured reflection coefficients of the square waveguide together with the rectangular-square transition, radiating into the free space, is below −25 dB in the desired frequency range (see Fig. 7).

2) Waveguide-Lens Matching: The impedance mismatch between the square waveguide feed and the HDPE lens can be minimized using the symmetric dielectric pin as shown in Fig. 1. The dielectric pins are milled on the focal plane

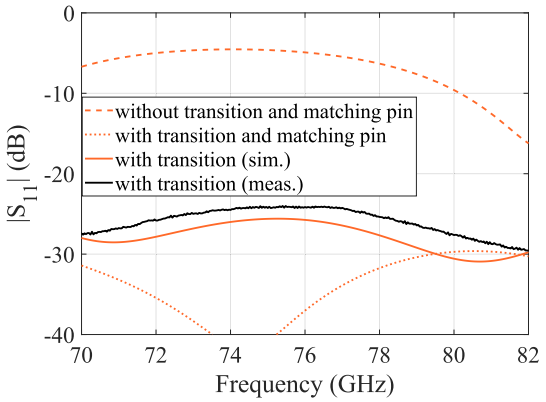

Fig. 7. The simulated (orange) and measured (black) reflection coefficients of the square waveguide feed radiating toward the dielectric half space (–/···) and free space (—). The square waveguide is fed with a WR-12 rectangular waveguide.

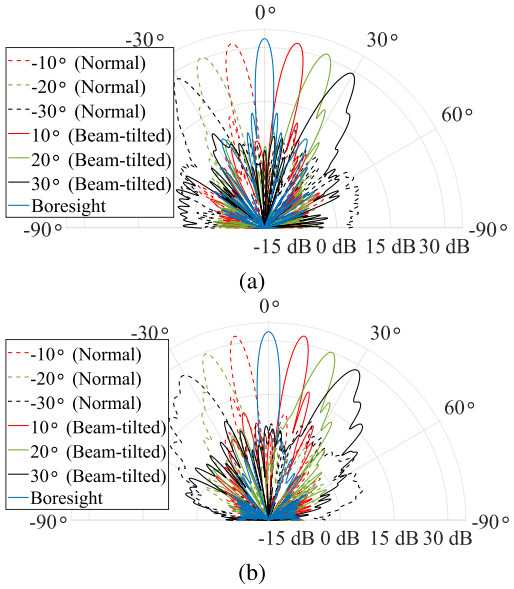

Fig. 8. Comparison of the simulated directivity radiation pattern of the IMLA with feed beam tilting: right and without beam tilting: left in the (a) H-plane and (b) E-plane at 73.5 GHz.

of the IMLA as shown in Fig. 1. The dielectric pin is symmetric trapezoid in shape. The height, top base, and bottom base dimensions are 2, 2.3, and 0.5 mm, respectively. The comparison of the feed reflection with and without the dielectric matching pin is depicted in Fig. 7. The addition of the transition and the dielectric pin lowers $|S_{11}|$ of the feed radiating into dielectric half-space below -30 dB in the entire range. The symmetric dielectric pin does not affect the radiation pattern of the feed.

D. Simulation of IMLA

The full-wave simulations of the IMLA are done with the 18-mm thick PVC ($\epsilon_r = 4$, $\tan\delta = 0.04$) support structure and the metal clamps. The simulated boresight directivity, D_{imla}, and gain, G_{imla}, of the IMLA are 32.5 dB and 31.8 dBi, respectively. The aperture efficiency, $\eta_a = 10^{(D_{imla}-D_{uni.})}$, and the radiation efficiency, $\eta_r = 10^{(G_{imla}-D_{imla})}$, of the IMLA are greater than 50% and 83% in the whole frequency band. The aperture and the radiation efficiency of the IMLA peaks to 73% and 92% at 73 GHz and 75 GHz, respectively. The internal reflections of the IMLA lower the directivity and aperture efficiency of the IMLA. The good radiation efficiency is due to low material loss and negligible spillover loss. The simulated directivity radiation pattern of the IMLA along the H- and E-planes is shown in Fig. 8(a) and (b), respectively. At 73.5 GHz, the half power beam width in the E-plane and H-plane of the boresight beam are 4.6° and 3.9°, respectively. The first side lobe level is at -27.6 dB and -20.5 dB along the E-plane and H-plane, respectively. The difference of beam width and SLL between the E- and H-planes is due to the narrower radiation pattern along the E-plane of the square waveguide feed when compared to the H-plane (see Fig. 6). The addition of the dielectric–metal and metal–plate to air matching layers improves the simulated gain of the IMLA by approx. 1.4 dB at boresight and higher steering angles.

III. Scan Loss Reduction

The far-field radiation pattern of an antenna is determined by the aperture amplitude and phase distribution. For a given aperture, the directivity is maximum when the amplitude across the radiating aperture is uniform. In the case of a lens antenna, as the feed moves away from the focal center, the amplitude and phase distribution across the radiating aperture becomes less-uniform which increases SLL and reduces the directivity in the far-field radiation pattern. In this work, the amplitude distribution along the lens aperture can be improved by tilting the radiation pattern of the offset feeds toward the center of the radiating aperture.

The tilting of the feed radiation pattern has various effects on an ILA performance. First, the beam tilting focuses more power to the regions of collimating surface where the angle of incidence is small, therefore the reflection loss decreases. In addition, the tilted beam from the focal plane improves the amplitude distribution across the radiating aperture. Both the above-mentioned effects improve the directivity of the lens. Furthermore, the tilting of the feed radiation pattern minimizes the power going toward the extension section. The spillover loss therefore decreases and gain improves. In this work, the improvement due to beam tilting is presented with the IMLA but the method can be applied to other dielectric ILAs as well.

A. Beam Tilting

A waveguide is one of the most commonly used feed antenna of an ILA. The radiation pattern of a waveguide is generally directed along the direction normal to the radiating aperture. In this work, the radiation pattern of a waveguide is tilted away from normal of the aperture by introducing an asymmetrical dielectric pin as shown in Fig. 1. The feed radiation pattern is simulated considering the feed radiating into the HDPE background material.

The amplitude distribution of the TE10 mode along the E- and H-plane of the square waveguide is different. In the

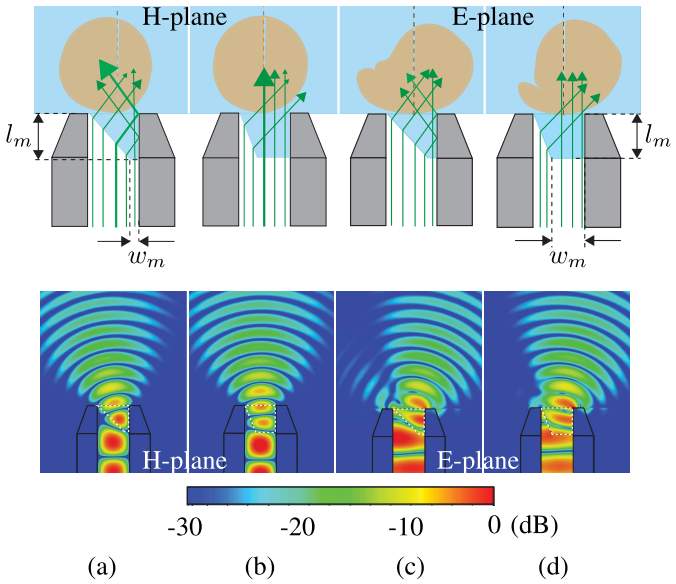

Fig. 9. Simplified ray illustration (top) and electric-field distribution (bottom) of the square waveguide along the H-plane (a, b) and E-plane (c, d) with the asymmetric dielectric pins at 73.5 GHz. The ray illustration (green), radiation patterns (yellow), and e-field distribution are presented for the dielectric pins designed to tilt the main beam to 12°, $l_m = 2.5$ mm, $w_m = 0.5$ mm (a, c), and 15°, $l_m = 2.5$ mm, $w_m = 2$ mm (b, d), in H- and E-planes, respectively. Note that the waveguide radiates to the same dielectric material as the pin is made of.

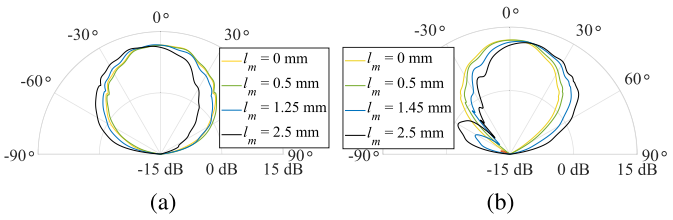

Fig. 10. Beam tilting of the square waveguide along (a) H-plane when $w_m = 0.5$ mm and (b) E-plane when $w_m = 2$ mm w.r.t. length l_m of the asymmetric dielectric pin at 73.5 GHz.

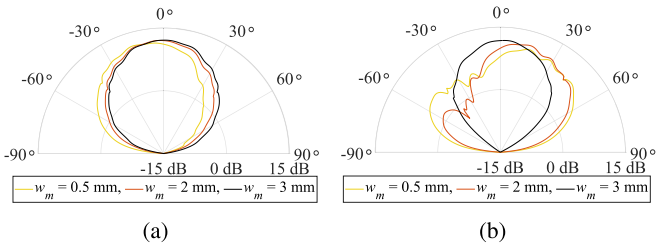

Fig. 11. Beam tilting of the square waveguide along (a) H-plane and (b) E-plane w.r.t. bottom width w_m when $l_m = 2.5$ mm of the asymmetric dielectric pin at 73.5 GHz.

case of the H-plane, the field amplitude is maximum near the waveguide axis and the amplitude gradually decreases toward the metallic wall. Therefore, the fields along the center with maximum amplitude plays a dominant role in determining the direction of the beam tilting. In the case of the E-plane, the amplitude distribution is uniform and all the fields have equal weight in determination of the beam-tilting angle and direction.

The beam tilting can be best understood by the principle of refraction and reflection. The electric-field travelling along the axis of the waveguide refracts when arrives on the slanted dielectric interface of the asymmetric pin. A part of the refracted field directly radiates, whereas the remaining field reflects from the waveguide wall and then radiates as shown in Fig. 9. The sum of the refracted and reflected fields on the waveguide aperture determines the beam-tilting angle and direction.

The amount of reflected and refracted field on the waveguide aperture can be controlled by the slant angle of the dielectric pin. The slanting angle is determined by the height l_m and bottom width w_m of the dielectric pin. The effect of the l_m and w_m on the beam tilting along the H-plane of a square waveguide is illustrated in Figs. 10(a) and 11(a), respectively. When, $l_m < 0.5$ mm, the fields mostly refract and radiate, without reflection. The direction of main beam tilt is small but toward positive θ. As the l_m increases, the angle of inclination increases and the reflected fields from the waveguide wall is larger. Therefore, the beam tilts toward negative θ. The maximum beam tilt of 12° is achieved with 2.5 mm height of the dielectric pin. The beam-tilting angle starts to saturate when l_m is greater than 2.5 mm. The smallest bottom width of the dielectric pin, $w_m = 0.5$ mm, gives the maximum beam-tilting angle. As w_m increases, larger proportion field passes through flat surface of the dielectric pin without refracting and reflecting which reduces the beam-tilting angle as illustrated in Figs. 9(b) and 11(a).

In the case of E-plane, as the length of the dielectric pin increases the tilt of the main lobe increases, toward positive θ. The main lobe direction is toward positive θ because the majority of the refracted fields are not reflected from the waveguide wall. However, as the l_m increases the proportion of reflected fields also increase, hence the sidelobe appear toward $\theta = -60°$. In order to limit the SLL below -10 dB, the $l_m = 2.5$ mm is chosen. The wider bottom width, w_m, helps minimize the amount of reflected field and reduce the SLL, although it slightly decreases the beam-tilting angle [see Fig. 9(c) and (d)]. Fig. 11(b) shows that when w_m is smaller, both the main lobe tilt angle and the SLL are higher. Therefore, $w_m = 2$ mm is chosen to minimize the SLL.

B. Scanloss Improvement

In this work, the main beam is steered to ±10°, ±20°, and ±30° along both the E- and H-planes of the IMLA. In order to achieve the steering angles, the square waveguide feeds are placed at ±5, ±10, and ±15 mm from the focal center along both axes as shown in Fig. 12. The dielectric pins are machined at the square waveguide feed positions to serve two purposes: improve matching and the feed beam tilting. The symmetric dielectric pins that are used at the center and along the positive x- and y-axes are designed to achieve low $|S_{11}|$ and it has the same dimensions at all locations. The asymmetric dielectric pins that are along the negative x- and y-axes are designed to achieve the feed beam tilt. The shape of the asymmetrical dielectric pin also affects the reflection coefficient $|S_{11}|$ of the square waveguide feed. In general,

TABLE I
DIMENSIONS OF FEED DIELECTRIC PINS AND IMLA RADIATION PROPERTIES AT 73.5 GHZ WITH/WITHOUT BEAMTILT

Direction	Offset position (mm)	w_m (mm)	l_m (mm)	Feed beam-tilt (°)	Steering angle (°)	Directivity (dB)	Gain (dBi)	SLL (dB)
E-plane	5	2/0.5	1.45/2	8/0	10/-10	32.2/31.9	31.7/31.4	14.7/16
	10	2/0.5	2.6/2	15/0	20/-20	30.7/30.2	29.9/29.4	13.5/9.5
	15	2/0.5	2.6/2	15/0	30/-30	28.5/26.8	27.5/25.6	7/3.8
H-plane	5	0.5/0.5	1.25/2	4/0	10/-10	32/32	31.1/31.1	21.6/20
	10	0.5/0.5	2.5/2	12/0	20/-20	31.2/30.3	30.1/29.2	15.6/12.4
	15	0.5/0.5	2.5/2	12/0	30/-30	29.2/27.8	27.7/26	9.7/7
Boresight	0	0.5/0.5	2/2	0	0	32.5	31.85	20.5

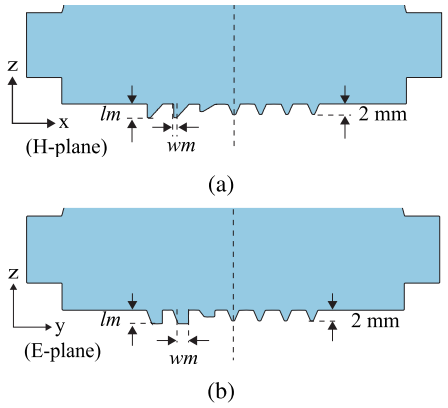

Fig. 12. Symmetric: reference feeds along the positive X- and Y-axes; asymmetric: beam-tilting feeds along the negative X- and Y-axes, arrangement along the focal plane of the IMLA for the (a) H-plane and (b) E-plane beam steering.

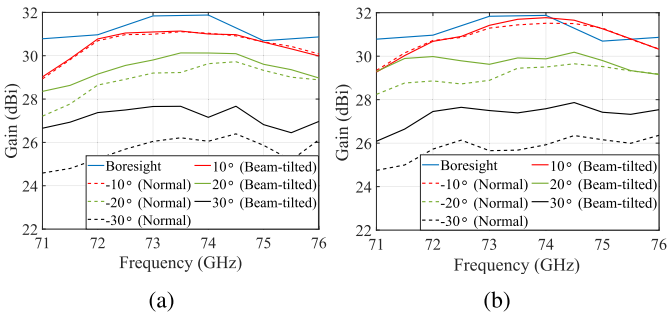

Fig. 13. Comparison of the simulated peak gain of the IMLA with (—) and without (- -) feed-beam tilting in the (a) H-plane and (b) E-plane.

the asymmetrical dielectric pin with larger l_m and smaller w_m has better matching performance.

Based on the IMLA geometry, at 5-, 10-, and 15 mm feed offset positions, the required beam-tilting angles are approx. 6.3°, 12.6°, and 19°, respectively. The height of the dielectric pins is increased with offset position to achieve the desired beam tilt. The exact dimensions of the feed pins are listed in Table I. As mentioned in the previous section, the maximum achievable feed beam tilts in the H-plane and E-plane are 12° and 15°, respectively. Therefore, the dimensions of the asymmetrical pins at 10- and 15 mm offset position are the same. Thus, the feed beam tilting at 15 mm offset position is not optimal.

The simulated directivity radiation patterns along the E- and H-planes at 73.5 GHz are illustrated in Fig. 8(a) and (b), respectively. The far-field properties of the IMLA at various steering angles are presented in Table I. Along the H-plane, the asymmetric feed pin improves IMLA directivity by 0.3, 0.5, and 1.7 dB at 10°, 20°, and 30° steering angles, respectively. At 10°, the increase in directivity is negligible compared to higher steering angles because the amplitude distribution with symmetrical feed is close to ideal. Similarly, the first SLL is improved by 1.6, 3.2, and 2.7 dB at 10°, 20°, and 30° steering angles, respectively. The beam steering performance along the E- and H-planes is similar.

The simulated peak gain with respect to frequency is plotted in Fig. 13. The gain of the IMLA at boresight and all steering angles peaks at the designed frequency range. For 30°, the gain scan loss of the IMLA is 4.15 and 5.85 dB along the H-plane with and without feed beam tilt, respectively. At 20° and 30° steering angles, the gain improvement is approx. 0.3 dB higher than the directivity improvement. As the feed beam is tilted, less power is transmitted toward the extension section, and consequently the energy leaking and decaying in the lossy PVC support structure is smaller, which results in the gain improvement. At 30° steering angle, more than 1 dB of scanloss improvement is achieved in the entire lower E-band. The gain and radiation pattern of the IMLA can be further improved if the feed beam can be tilted further.

IV. COMPARISON AND DISCUSSION

In this section, the IMLA is compared with the state-of-the-art ILA designs based on the dimensions, efficiency, and scan loss properties. Three ILAs with similar design objectives, comparable diameter, and operation frequency to the IMLA are compared in Table II. The traditional dielectric lens in [11] is designed for optimal boresight gain with minimized scan loss, the shaped double-shell lens (SDSL) in [13] is designed for smaller height and low scan loss, and the double lens (DL) focusing system in [22] is designed to minimize the scan loss.

The f/d ratio of a traditional ILA is close to 1 and the aperture efficiency is more than 90%. Though an elliptical ILA has high aperture efficiency, the spillover loss and dielectric loss reduce the radiation efficiency. The SDSL design in [13] uses the multiple dielectrics to minimize the f/d (0.785) and scan loss (0.4 dB). The aperture and radiation efficiency of the SDSL are 38% and 24%, respectively. The low radiation efficiency is caused by the higher loss tangent of the material used in SDSL fabrication. The IMLA can also be considered as multi dielectric lens with the combination of dielectric lens

TABLE II
COMPARISON OF THE SIMULATED IMLA CHARACTERISTICS WITH THE STATE-OF-THE-ART ILA

References	Elliptical [11]	SDSL [13]	DL [22]	IMLA
Diameter (λ)	16	12.5	16	16
Frequency (GHz)	73.5	62.5	77	73.5
Height (λ)	17.82	9.8	16.87	11.1
f/d (elliptical)	1.1	0.785	1.05 (0.97)	0.69 (1.11)
ϵ_r (tanδ)	2.53 (0.0013)	5.5/2.53 (0.0021/ 0.0047)	3 (0.003)	2.3 (0.0002)
Aperture efficiency η_a, (%)	91	38	53	73
Radiation efficiency η_r, (%)	34	24	56	92
Boresight gain, dBi (uni. illuminated)	29.1 (34)	18.3 (31.88)	28.7 (34)	31.9 (34)
Offset gain, dBi (steering angle)	23.8 (24°)	18.4 (20.1°)	27.5 (30°)	27.7 (30°)

($\epsilon_r > 1$) and metal–plate lens ($\epsilon_r < 1$) that reduces the f/d to 0.69. The effective permittivity of the metal–plate lens can be tuned by varying separation distance a and losses in the metal–plate lens is minimal. The IMLA gives freedom to design with any dielectric material with low loss tangent. Therefore, a good radiation efficiency can be achieved, as 92% for the designed IMLA verifies.

The scanloss performance of the designed IMLA for 30° steering angle without beam tilting is 5.8 dB, which is better in comparison to a traditional dielectric ILA, that is, approx 7.4 dB. The scan loss of the IMLA with feed beam tilting, 4.1 dB at 30°, is higher than that of the SDSL, 0.4 dB at 20°, the DL, 1.2 dB at 30°, and the dual-spherical lens, 1.3 dB at 40° [25]. However, the absolute gain at 30° steering angle of the proposed IMLA, that is, 27.7 dBi, is better than that of the DL, that is, 27.5 dBi. The radiation efficiency of DL can be improved with low-loss material like Teflon and HDPE, but a low permittivity material might further increase the f/d of the DL. The improved scanning property of the designed IMLA is due to the tilted feed radiation pattern and higher efficiency.

In this section, the simulation results of the IMLA are compared with those of the other state-of-the-art ILA designs. The simulation results represent the optimal performance of the proposed ILA designs, which excludes the effects of the manufacturing inaccuracies. The manufacturing challenges can be overcome with more experience and new and better fabrication technologies.

V. IMLA FABRICATION AND MEASUREMENT

The manufacturing process of 16-λ_0 IMLA with 11.1-λ_0 focal length is discussed in this section. The dielectric lens is manufactured by machining the HDPE material. The picture of the machined HDPE lens with feed pins and dielectric–metal matching layer is presented in Fig. 14(a).

The metal–plate lens is manufactured by the intersection of the 58 laser-cut individual stainless steel plates. The assembly of the stainless steel plates with the same 50-μm plate thickness and intersecting slot width is challenging. The inaccuracies of laser cutting and lack of tolerance margin in addition to the flexibility of the steel plates made the intersecting assembly impossible in practice.

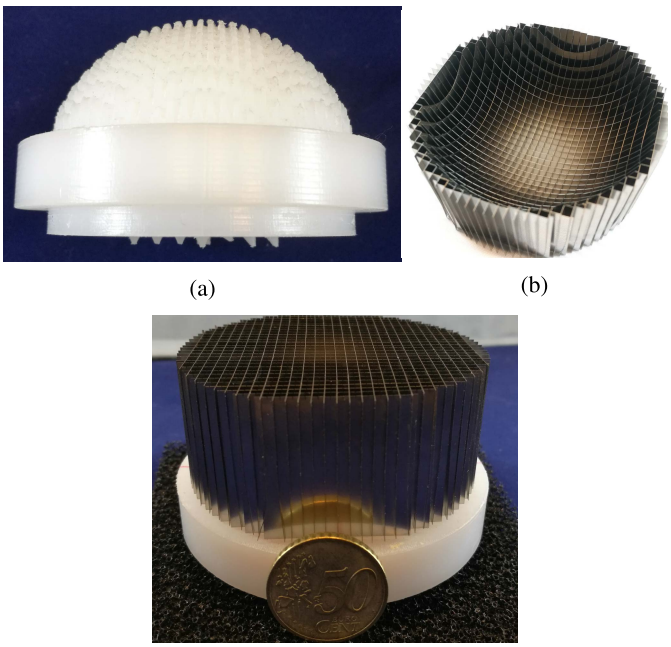

Fig. 14. (a) The dielectric lens, (b) the metal–plate lens, and (c) the combination of metal–plate lens (top) and dielectric lens (bottom) to form the IMLA.

To overcome the mentioned difficulties and to ease the assembly, the thickness of the steel plates and the width of the intersecting slots are increased. For the same IMLA design, the thickness of the steel plates was increased to 80 μm and the intersecting slot width was increased to 105 μm. The assembled metal–plate lens is shown in Fig. 14(b). The change in dimension eased the assembly of the metal–plate lens. However, the increase in plate thickness decreases the effective waveguide width and consequently the ϵ_m decreases. Therefore, the operating frequency of the IMLA shifts toward the higher frequency as shown later in this section.

The metal–plate lens is positioned on top of the dielectric lens, as shown in Fig. 14(c). The PVC support structure and 0.5 mm thick stainless steel clamp are used to position the IMLA [see Fig. 15(c)].

Before the S-parameter measurements, the one-port calibration is done by establishing the reference point at the end of WR-12 waveguide of the extender. The square waveguide feed is connected to the VNA extender using the rectangular–square transition plates. The reflection coefficients are measured by placing the square waveguide feed at different offset positions of the IMLA, as shown in Fig. 15(b). For all offset positions, the simulated and measured $|S_{11}|$ is below -10 dB in the entire band of interest, that is, 71–76 GHz, and extends between 70 and 82 GHz (see Fig. 16). The offset feed ports with asymmetric dielectric pins have higher $|S_{11}|$ as they are optimized for maximum beam tilt, in contrary to the symmetric dielectric pins, which are designed for lower $|S_{11}|$. The center

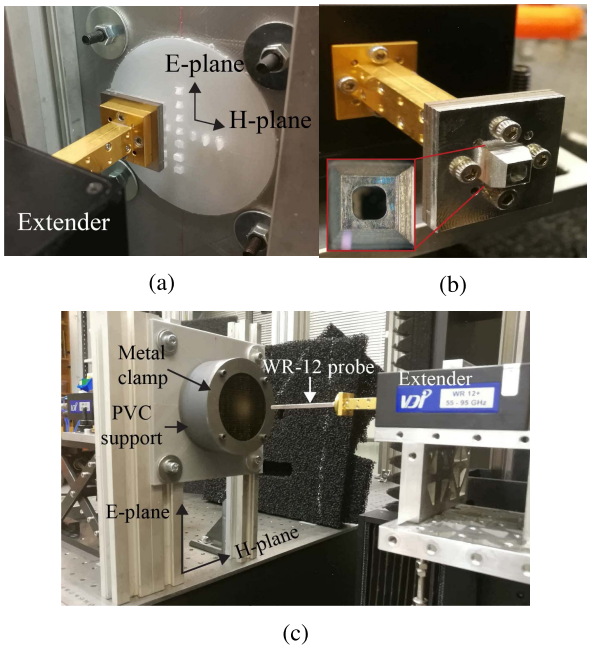

Fig. 15. (a) Focal plane of the IMLA with dielectric feed pins, (b) fabricated square waveguide feed with transitions, and (c) measurement setup of the IMLA in a planar near-field scanner.

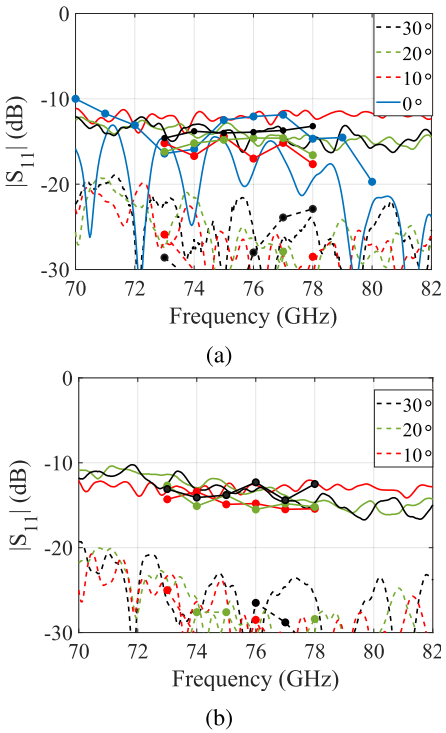

Fig. 16. Comparison between the measured and simulated $|S_{11}|$ of the IMLA with beam-tilting (—) and without beam-tilting (- -) feeds along (a) H-plane and (b) E-plane. The simulation results are presented as a scatter plot with circular markers.

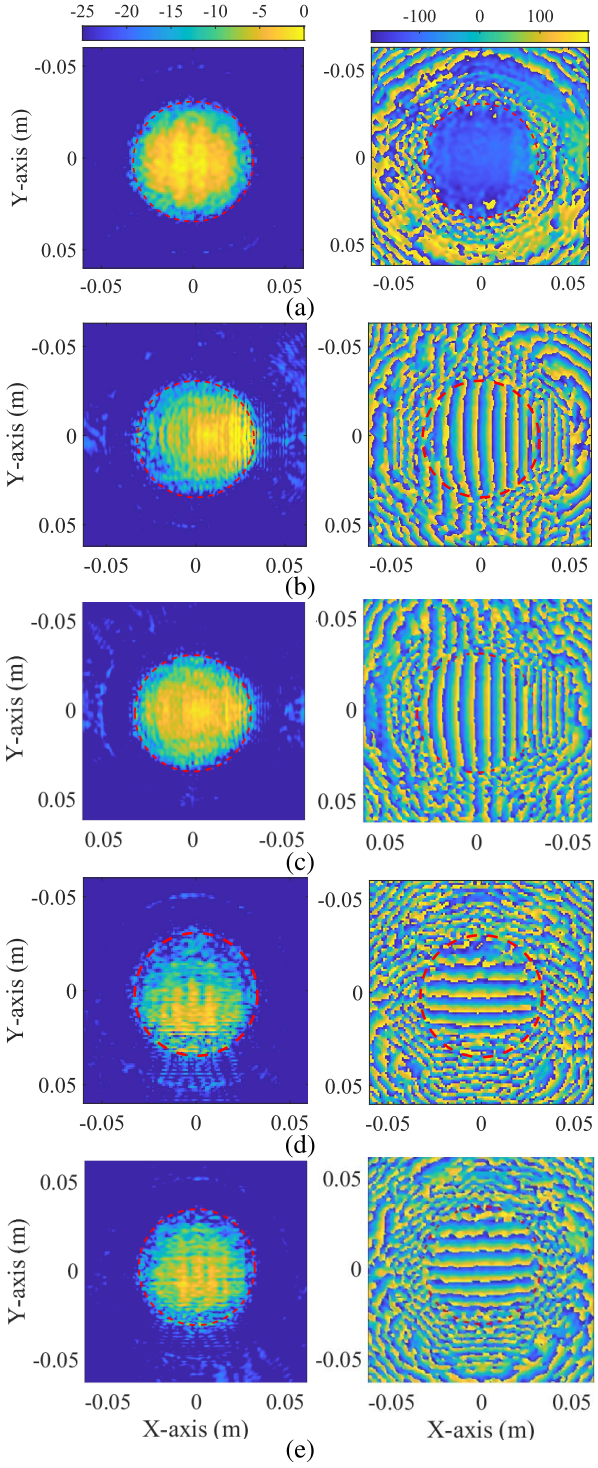

Fig. 17. Electric-field amplitude (left) and phase (right) pattern at the aperture of the IMLA while radiating toward (a) boresight, (b) −30° H-plane, (c) 30° H-plane (tilted feed beam), (d) −30° E-plane, and (e) 30° E-plane (tilted feed beam) at 76 GHz. The dashed red line depicts the radiating aperture of the IMLA. (c) and (e) Rotated 180° to ease comparison with (b) and (d), respectively.

feed or the boresight beam has maximum $|S_{11}|$ because the reflected field from the dielectric–metal interface converges at the focal point.

The radiation pattern and gain of the IMLA are measured in a planar near-field scanner at a frequency range between 70 and 82 GHz, as shown in Fig. 15(b). Fig. 17 shows the back-propagated E-field pattern at the radiating aperture (inside red dashed line) of the IMLA, which are calculated from the measured near-field with the feeds at various offset positions. The aperture amplitude is normalized with respect

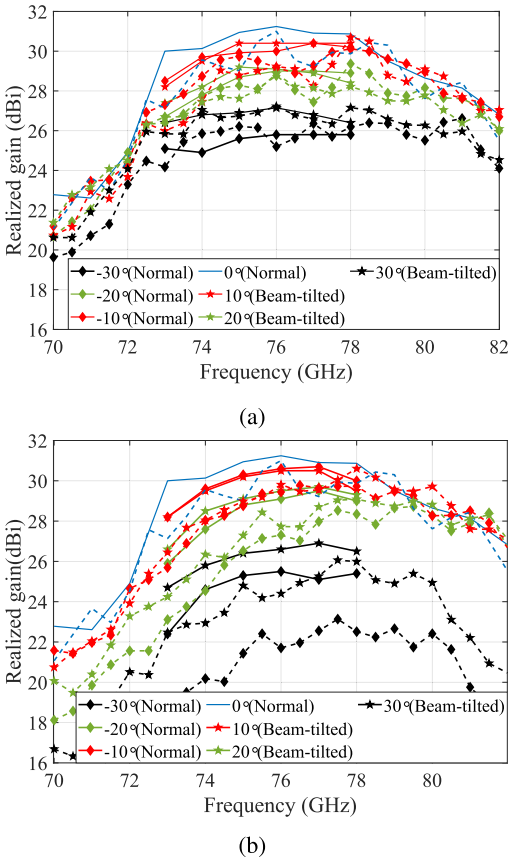

Fig. 18. Comparison of the simulated (—) and measured (- -) peak IMLA realized gain along (a) H-plane and (b) E-plane with (-⋆-) and without (-◆-) feed beam tilting.

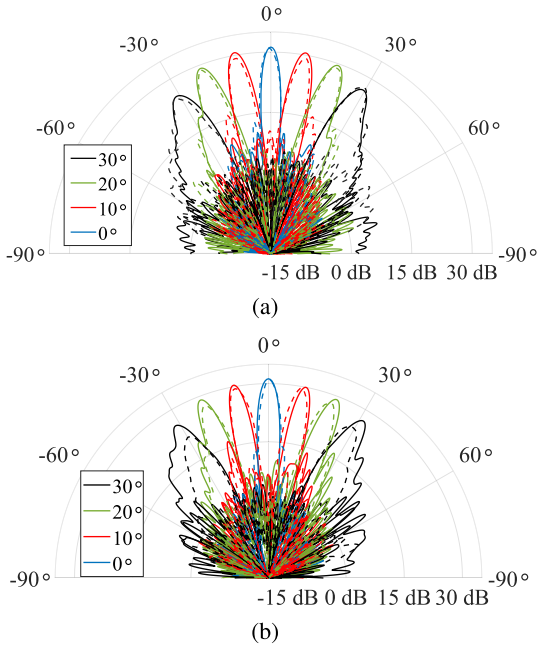

Fig. 19. Comparison between the simulated (—) and measured (- -) radiation patterns of the IMLA with beam tilt: right and without beam tilt: left, along the (a) H-plane and (b) E-plane at 76 GHz.

to peak aperture amplitude when the IMLA is radiating toward the boresight. The amplitude pattern shows that most of the waveguide elements of the metal–plate lens are working as expected. In Fig. 17(c) and (e), the amplitude distribution along the radiating aperture is more uniform as compared to Fig. 17(b) and (d), respectively. The improvement in the field distribution is due to the feed beam tilt along the H-plane and E-plane. The hologram image of the IMLA shows only slight spurious radiation leaking from the gap between the PVC and the metal clamp. The normalized amplitude of the leakage is approx. −20 dB, and therefore, the effect in radiation pattern and gain should be minimal.

The measured peak realized gain of the IMLA, when the main beam is directed to boresight, shows close agreement with the simulation results [see Fig. 18(a)]. Both simulated and measured realized gain peaks at 76 GHz instead of 73.5 GHz due to increased plate thickness and increased the intersection slot width. At 76 GHz, the measured and simulated realized gains of the IMLA are 31 dBi and 31.2 dB, respectively. The measured −3 dB gain bandwidth of the IMLA ranges between 73.5 and 81 GHz, that is, 9.9% gain bandwidth. The measured radiation pattern of the IMLA is in close agreement with the simulated ones [see Fig. 19(a)]. At 76 GHz, the measured half-power beamwidth is 4° in both the planes. Similarly, the measured first SLL along the H- and E-planes are −18.3 and −17.5 dB, respectively.

When the main beam is steered along the H-plane of the IMLA, the measured results closely follow the simulation results. For 30° steering angle with the normal feed, the simulated and measured scan loss is 5.4 and 5.8 dB, respectively. The simulated and measured scan loss decrease to 4 and 3.8 dB, respectively, at 76 GHz with the tilted feed radiation pattern. When the beam is steered to 30°, the feed radiation pattern tilting improves both the measured and simulated scan loss by approx. 1 dB between 73 and 78 GHz. At 10° and 20° steering angles, the improvement in scan loss is negligible. The measured and simulated off-axis radiation patterns of the IMLA are in congruence [see Fig. 19(a)]. The minor difference between the simulation and measured realized gains for 0°, 10°, 20°, and 30° steering angles along the H-plane could be caused by error in assembly of 58 metal–plates.

The comparison between the measured and simulated IMLA peak realized gains and radiation patterns while steering along the E-plane is shown in Figs. 18(b) and 19(b), respectively. The difference between the simulated and measured realized gains increases with increasing steering angle. Possible reasons for the differences are: 1) shift in operating frequency of the metal–plate lens and 2) radiation pattern distortion and increase in cross-polar radiation of the square waveguide feed.

Fig. 18(b) illustrates that, for the beams steered along the E-plane, except for −30° steering with normal feed, the peak gain differences between simulations and measurements are less than 1 dB. However, the measured gains peak at 1–2 GHz higher frequency. The shift in operating frequency is associated with the lack of contact between the orthogonally placed metal plates, which is caused by the difference in the plate thickness (80 μm) and intersecting slot width (105 μm). The thickness of the fabricated stainless steel plates seem to

be accurate, however inaccuracies in the laser-cut slot width dimensions were observed while inspecting with microscope. The simulation study shows that the larger gaps between the metal plates increase the operation frequency of the IMLA.

For $-30°$ steering along the E-plane with normal feed, the 2–3 dB gain difference between the simulation and measured gains is potentially due to the deformation of the fabricated square waveguide, as shown in Fig. 15(b). The measured aperture field shown in Fig. 17(d) illustrates higher under illumination in the upper half of the radiating aperture, whereas the strong stray radiations are present toward the lower edge, as compared to the simulations. Fig. 6 shows that the deformation of the square waveguide generates the asymmetric radiation pattern along the E-plane. The possible orientation of the square waveguide radiation toward the edge of the radiating aperture could be the reason for the higher under illumination and stray radiation which consequently decreases the measured IMLA gain. Second, the deformed square waveguide radiates higher cross-polar components toward the higher elevation angles along the E-plane. The evaluation of cross-polarized back-propagated aperture fields of the IMLA expose that, for $-30°$ steering angle along the E-plane, the measured loss due to cross-polarization radiation is 0.55 dB higher than in the simulations.

The measured peak cross-polarization discrimination (XPD) of the IMLA is 21 dB when the main beam is directed toward the boresight. At 30° steering angle along the E-plane, the XPD is 19.8 and 14.25 dB with and without the beam tilting.

Apart from the differences, the simulated and measured radiation pattern comparisons demonstrate the good agreement in terms of the beam steering direction, HPBW, and first SLL. The feed radiation pattern tilting along the E-plane helps improve the peak realized gain by more than 0.5 dB and 3 dB at 20° and 30° steering angle, respectively.

VI. Conclusion

A 16-λ_0 diameter IMLA is designed, fabricated, and characterized at the E-band. The peak aperture and radiation efficiency of the designed IMLA are 73% and 92%, respectively. The IMLA has measured realized gain of 31 dBi toward boresight direction at 76 GHz. For 30° steering angle along the H-plane, the measured scan loss of the IMLA with and without beam tilting is 3.8 and 5.8 dB, respectively.

The simulation and measurement results show that the proposed IMLA is efficient and low-profile. The scan loss of the proposed design is smaller than a traditional ILA. Further improvement in scan loss is achieved by tilting the feed radiation pattern.

Acknowledgment

The authors would like to thank Matti Vaaja for his support in the fabrication of PVC support structure and dielectric lens.

References

[1] D. F. Filipovic, S. S. Gearhart, and G. M. Rebeiz, "Double-slot antennas on extended hemispherical and elliptical silicon dielectric lenses," *IEEE Trans. Microw. Theory Techn.*, vol. 41, no. 10, pp. 1738–1749, Oct. 1993.

[2] D. F. Filipovic, G. P. Gauthier, S. Raman, and G. M. Rebeiz, "Off-axis properties of silicon and quartz dielectric lens antennas," *IEEE Trans. Antennas Propag.*, vol. 45, no. 5, pp. 760–766, May 1997.

[3] S. K. Karki, J. Ala-Laurinaho, V. Viikari, and R. Valkonen, "Lens antenna design for E-band point-to-point radio links," in *Proc. Prog. Electromagn. Res. Symp. Spring (PIERS)*, May 2017, pp. 1625–1631.

[4] J. R. Costa, E. B. Lima, and C. A. Fernandes, "Compact beam-steerable lens antenna for 60-GHz wireless communications," *IEEE Trans. Antennas Propag.*, vol. 57, no. 10, pp. 2926–2933, Oct. 2009.

[5] M. K. Saleem, H. Vettikaladi, M. A. S. Alkanhal, and M. Himdi, "Lens antenna for wide angle beam scanning at 79 GHz for automotive short range radar applications," *IEEE Trans. Antennas Propag.*, vol. 65, no. 4, pp. 2041–2046, Apr. 2017.

[6] J. Ala-Laurinaho *et al.*, "2-D beam-steerable integrated lens antenna system for 5G E-band access and backhaul," *IEEE Trans. Microw. Theory Techn.*, vol. 64, no. 7, pp. 2244–2255, Jul. 2016.

[7] A. Artemenko, A. Mozharovskiy, A. Maltsev, R. Maslennikov, A. Sevastyanov, and V. Ssorin, "Experimental characterization of E-band two-dimensional electronically beam-steerable integrated lens antennas," *IEEE Antennas Wireless Propag. Lett.*, vol. 12, pp. 1188–1191, 2013.

[8] J. Ala-Laurinaho, A. Karttunen, J. Säily, A. Lamminen, R. Sauleau, and A. V. Räisänen, "Mm-wave lens antenna with an integrated LTCC feed array for beam steering," in *Proc. 4th Eur. Conf. Antennas Propag.*, Apr. 2010, pp. 1–5.

[9] A. Karttunen, J. Ala-Laurinaho, R. Sauleau, and A. V. Räisänen, "Reduction of internal reflections in integrated lens antennas for beam-steering," *Prog. Electromagn. Res.*, vol. 134, pp. 63–78, 2013.

[10] N. T. Nguyen, N. Delhote, M. Ettorre, D. Baillargeat, L. Le Coq, and R. Sauleau, "Design and characterization of 60-GHz integrated lens antennas fabricated through ceramic stereolithography," *IEEE Trans. Antennas Propag.*, vol. 58, no. 8, pp. 2757–2762, Aug. 2010.

[11] S. K. Karki, J. Ala-Laurinaho, A. Karttunen, and V. Viikari, "Integrated lens antennas for E-band," in *Proc. 48th Eur. Microw. Conf. (EuMC)*, Sep. 2018, pp. 1151–1154.

[12] M. Imbert, J. Romeu, M. Baquero-Escudero, M. Martinez-Ingles, J. Molina-Garcia-Pardo, and L. Jofre, "Assessment of LTCC-based dielectric flat lens antennas and switched-beam arrays for future 5G millimeter-wave communication systems," *IEEE Trans. Antennas Propag.*, vol. 65, no. 12, pp. 6453–6473, Dec. 2017.

[13] J. R. Costa, M. G. Silveirinha, and C. A. Fernandes, "Evaluation of a double-shell integrated scanning lens antenna," *IEEE Antennas Wireless Propag. Lett.*, vol. 7, pp. 781–784, 2008.

[14] J. R. Costa, C. A. Fernandes, G. Godi, R. Sauleau, L. Le Coq, and H. Legay, "Compact Ka-band lens antennas for LEO satellites," *IEEE Trans. Antennas Propag.*, vol. 56, no. 5, pp. 1251–1258, May 2008.

[15] R. Sauleau and B. Bares, "A complete procedure for the design and optimization of arbitrarily shaped integrated lens antennas," *IEEE Trans. Antennas Propag.*, vol. 54, no. 4, pp. 1122–1133, Apr. 2006.

[16] N. T. Nguyen, A. Rolland, A. V. Boriskin, G. Valerio, L. L. Coq, and R. Sauleau, "Size and weight reduction of integrated lens antennas using a cylindrical air cavity," *IEEE Trans. Antennas Propag.*, vol. 60, no. 12, pp. 5993–5998, Dec. 2012.

[17] M. R. D. Kodnoeih, Y. Letestu, R. Sauleau, E. M. Cruz, and A. Doll, "Compact folded Fresnel zone plate lens antenna for mm-wave communications," *IEEE Antennas Wireless Propag. Lett.*, vol. 17, no. 5, pp. 873–876, May 2018.

[18] A. Mozharovskiy, A. Artemenko, O. Soykin, and R. Maslennikov, "Lens array antenna for 71–76/81–86 GHz point-to-point applications," in *Proc. 46th Eur. Microw. Conf. (EuMC)*, Oct. 2016, pp. 413–416.

[19] S. K. Karki, J. Ala-Laurinaho, and V. Viikari, "Integrated metal-lens antennas with reduced height at 71–76 GHz," in *Proc. 13th Eur. Conf. Antennas Propag. (EuCAP)*, Mar. 2019, pp. 1–5.

[20] A. V. Boriskin and R. Sauleau, "Numerical investigation into the design of shaped dielectric lens antennas with improved angular characteristics," *Prog. Electromagn. Res. B*, vol. 30, pp. 279–292, 2011.

[21] N. T. Nguyen, M. Casaletti, T. V. La, and R. Sauleau, "Synthesized elliptical lens with optimized extension for focal array fed lens antennas," in *Proc. 6th Eur. Conf. Antennas Propag. (EUCAP)*, Mar. 2012, pp. 3295–3298.

[22] N. T. Nguyen, A. V. Boriskin, L. Le Coq, and R. Sauleau, "Improvement of the scanning performance of the extended hemispherical integrated lens antenna using a double lens focusing system," *IEEE Trans. Antennas Propag.*, vol. 64, no. 8, pp. 3698–3702, Aug. 2016.

[23] M. J. M. van der Vorst, P. J. I. de Maagt, and M. H. A. J. Herben, "Scan-optimized integrated lens antennas," in *Proc. 27th Eur. Microw. Conf.*, vol. 1, Sep. 1997, pp. 605–610.

[24] A. Karttunen, J. Ala-Laurinaho, R. Sauleau, and A. V. Räisänen, "Extended hemispherical integrated lens antenna with feeds on a spherical surface," in *Proc. 7th Eur. Conf. Antennas Propag. (EuCAP)*, Apr. 2013, pp. 2539–2543.
[25] A. E. I. Lamminen, A. Karttunen, M. Kaunisto, J. Saily, and M. Lahdes, "Beam-switching dual-spherical lens antenna with low scan loss at 71–76 GHz," *IEEE Antennas Wireless Propag. Lett.*, vol. 17, no. 10, pp. 1871–1875, Oct. 2018.
[26] G. C. Trichopoulos, G. Mumcu, K. Sertel, H. L. Mosbacker, and P. Smith, "A novel approach for improving off-axis pixel performance of terahertz focal plane arrays," *IEEE Trans. Microw. Theory Techn.*, vol. 58, no. 7, pp. 2014–2021, Jul. 2010.
[27] M. A. Campo, G. Carluccio, S. Bruni, and N. Llombart, "Dielectric gratings enhancing the field of view in low dielectric permittivity elliptical lenses," *IEEE Trans. Antennas Propag.*, early access, May 5, 2021, doi: 10.1109/TAP.2021.3076524.
[28] W. E. Kock, "Metal-lens antennas," *Proc. IRE*, vol. 34, no. 11, pp. 828–836, Nov. 1946.

Sabin Kumar Karki (Student Member, IEEE) was born in Kathmandu, Nepal, in 1988. He received the B.E. degree in electronics and communication engineering from Tribhuwan University, Kirtipur, Nepal, in 2010, and the M.Sc. (Tech.) degree in radio science and engineering from Aalto University, Aalto, Finland, in 2016, where he is currently pursuing the Ph.D. degree in radio engineering.

He joined the Department of Electronics and Nanoengineering, Aalto University, as a Research Assistant in 2016. His current research interest includes millimeter-wave beam steering antennas, such as lens antenna and antenna array.

Juha Ala-Laurinaho received the Diploma Engineer (M.Sc.) degree in mathematics and the D.Sc. (Tech.) degree in electrical engineering from the TKK Helsinki University of Technology, Espoo, Finland, in 1995 and 2001, respectively.

He has been with TKK, currently Aalto University, serving in the Radio Laboratory from 1995 to 2007, in the Department of Radio Science and Engineering from 2008 to 2016, and currently in the Department of Electronics and Nanoengineering. Currently, he works as a Staff Scientist. He has been a researcher and project manager in many millimeter-wave technology-related projects. His current research interests are the antennas and antenna measurement techniques for millimeter and submillimeter waves, and the millimeter-wave imaging.

Ville Viikari (Senior Member, IEEE) was born in Espoo, Finland, in 1979. He received the Master of Science (Tech.) and Doctor of Science (Tech.) (Hons.) degrees in electrical engineering from Helsinki University of Technology (TKK), Espoo, in 2004 and 2007, respectively.

From 2001 to 2007, he was with the Radio Laboratory, TKK, where he studied antenna measurement techniques at submillimeter wavelengths and antenna pattern correction techniques. From 2007 to 2012, he was a Research Scientist and Senior Scientist with the VTT Technical Research Center, Espoo, where his research included wireless sensors, RFID, radar applications, MEMS, and microwave sensors. He is currently an Associate Professor and the Deputy Head of the department, School of Electrical Engineering, Aalto University, Espoo. His current research interests include antennas for mobile networks, RF-powered devices, and antenna measurement techniques.

Dr. Viikari was a recipient of the Young Researcher Award of the year 2014 presented by the Finnish Foundation for Technology Promotion, the IEEE Sensors Council 2010 Early Career Gold Award, the 2008 Young Scientist Award of the URSI XXXI Finnish Convention on Radio Science, Espoo, and the Best Student Paper Award of the Annual Symposium of the Antenna Measurement Techniques Association, Newport, RI, USA, from October 30 to November 4, 2005. He has served as the Chair for the Technical Program Committee of the ESA Workshop on Millimeter-Wave Technology and Applications and the Global Symposium on Millimeter Waves (GSMM) twice in 2011 and 2016, Espoo.